Iranian Journal of Science and Technology, Transactions of Civil Engineering (2021) 45:1441–1456
https://doi.org/10.1007/s40996-020-00434-5

RESEARCH PAPER

CFST Rib with Circumferential Gap and SWS Composite Defects

Chao Guo[1] · **Zhengran Lu**[1]

Received: 7 October 2019 / Accepted: 19 June 2020 / Published online: 4 July 2020

Abstract
Most large-diameter concrete-filled steel tube (CFST) arch bridges adopt spiral-welded steel tubes for technical and economic reasons. However, during the steel tube manufacturing process, the welding temperature and other factors lead to a decreased spiral-welded seam (SWS) strength, initially. Furthermore, harsh environments, especially in the cold regions of northern China, during service and concrete dry shrinkage cause the steel tube and core concrete circumferential gaps to constitute composite defects in CFST structures. This paper presents a group finite element model analysis of the bearing capacity of a serviced CFST arch bridge rib with a circumferential gap and decreased SWS strength under small eccentric axial compression, using ultrasonic scanning field experience. The nonlinear behavior of the constituent and the effect of composite defects on the CFST behavior are investigated. Parametric studies are conducted to investigate the influence of the composite defects on the bearing capacity of the rib. Finally, a new ultimate strength index of the rib is proposed for the composite defects, and a simplified formula is presented to estimate the effects of the circumferential gaps and SWS strength decrease on the ultimate strength of the CFST arch bridge rib.

Keywords Concrete-filled steel tube · Spiral-welded seam · Circumferential gap · Composite defect · Arch bridge

1 Introduction

In the past few decades, several concrete-filled steel tube (CFST) arch bridges, which have been used in China for many years (Zheng and Wang 2018), have formed part defects of the steel tube or concrete column imperfections during their service life or owing to initial construct. In harsh environments, particularly in the seasonal freeze–thaw zone where the temperature changes significantly, the depth of the interface gap deteriorates rapidly and expands, which shortens the bridge service life and may even finally lead to bridge collapse.

The Chang-Qing Hun River Bridge in Shenyang city, Liaoning province, in the north of China, is an important part of the southern express road system and is of great significance for the environmental protection and economic development of the Shenyang region. The bridge was constructed in 1997, as illustrated in Fig. 1.

The main bridge has a net span of 120 + 140 + 120 m. The bearing type of the Chang-Qing Hun River Bridge was a half-through CFST arch rib system. The height of the arch cross section is 2.4 m, and the arch width is 1.8 m. Each rib consists of four tubes with a diameter of 720 mm; the thickness of the spiral-welded tube (SWT) is 10 mm.

SWTs are fabricated by welding the resulting abutting edges of a helically bending steel plate. The SWT is an economical tubing structure that can be used for long-span CFST arch bridge ribs. However, SWTs exhibit decreased welded seam strength compared to the base metal and therefore can be considered to have a single defect. Many tests have been conducted on concrete-filled SWT columns, considering short and long column behavior, to estimate the applicability of existing guidelines for evaluating their strength and failure types (Gunawardena and Aslani 2018; Gunawardena et al. 2019).

Owing to the limitations of technical levels over 20 years ago, the spiral-welded seam (SWS) only penetrated 70%. Therefore, during the 2012 maintenance process, a steel strip with an 80 mm width and 10 mm thickness was adopted to reinforce the welded seam of the bridge, as illustrated in

✉ Zhengran Lu
luzhengran@sjzu.edu.cn

Chao Guo
guochao@sjzu.edu.cn

[1] School of Civil Engineering, Shenyang Jianzhu University, Middle Hunnan Road, Shenyang 110168, China

Fig. 1 Chang-Qing Hun River Bridge

Fig. 2 Details of CFST arch

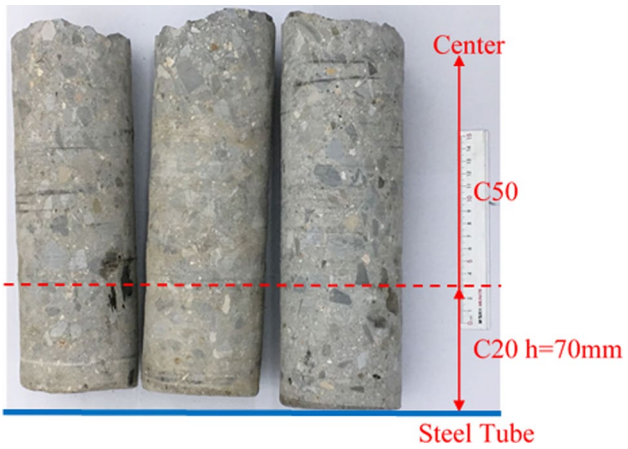

Fig. 3 Concrete segregating specimen in tube

Fig. 2. The transverse and K shape supports have the same diameter and thickness as the main arch ribs.

Currently, the concrete poured into the CFST arch ribs is self-consolidating concrete (SCC) owing to its convenience in construction. The filling ability, as the workability parameter, passing ability, and stability (aggregate segregation resistance) of SCC play key roles and should be checked in the initial mix proportion design. The separation resistance to maintain a uniform distribution of fine and coarse aggregates is one of the most important demands for SCC (Chen et al. 2018; Ramge et al. 2010). However, research into the application of SCC in CFST arch bridges began in China in 2001, four years after the completion of this bridge case (Ding et al. 2001); the concrete used in this bridge was ordinary concrete.

C50 concrete was designed to fill in the bridge tubes. However, owing to the limitations of the construction technology at that time, the concrete was segregated in the tube. According to the core-taking test conducted on site, the concrete strength was C20 within a range of 7 cm near the inner tube wall, as illustrated in Fig. 3.

The bridge was constructed in a region that experiences a relatively cold environment compared to the south of China, with five months of winter, which presents challenges associated with the mechanical sensitivity of engineering measures to temperature variations. Under the conditions of a seasonal frozen region at high latitudes, engineering structures are forced to consider the threat of subsidence resulting from frost heaving (Wang et al. 2013; Peng et al. 2017; Pan et al. 2018).

In response to such threats, in most cases, detecting the imperfections of the CFST appears to provide an effective approach for evaluating the stability of the CFST arch bridge in the seasonal frost region. This has been achieved by an ultrasonic three-dimensional (3D) section scanning imager, MIRA A1040, made by ACSYS of Russia, and the results are presented in Fig. 4. The ratio of the interface gap area to the total tube area is approximately 3.6% to 30.5%, and the circumferential gap depth is approximately 5 to 15 mm. Ultrasonic nondestructive testing technology has been used extensively for the defect inspection of concrete structures in civil engineering. In particular, its reliability of test results has been proven by a large number of indoor tests on CFST

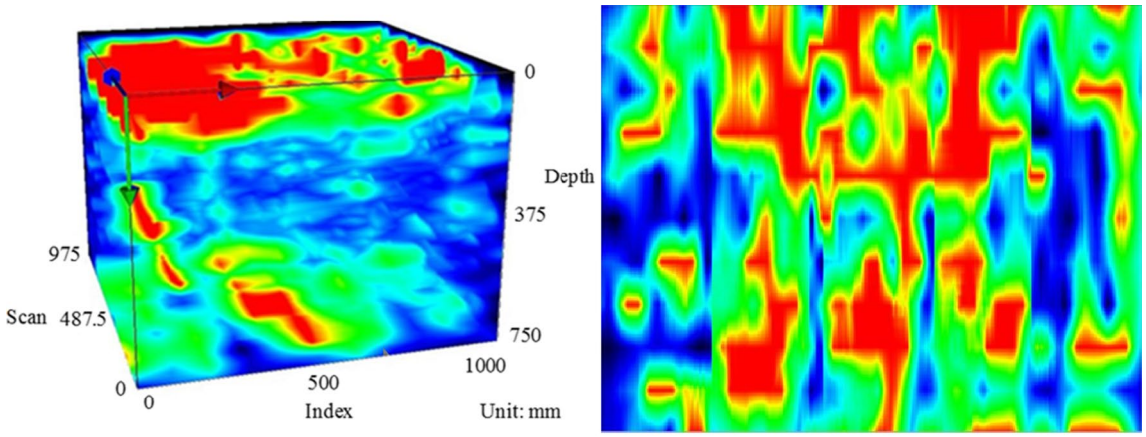

(a) 3D section scanning imagery **(b)** Plane scanning imagery

Fig. 4 Ultrasonic scanning imagery of CFST

defects (Liu et al. 2019; Yan et al. 2018; Dong et al. 2016; Ye et al. 2011).

In the past two decades, many numerical and experimental studies have been carried out on CFST ribs under axial loading using the finite element model (FEM) (Pham and Nguyen 2019; Pham et al. 2019). Han et al. (2007), Schneider (1998), Hu et al. (2003), and Ellobody and Young (2006a, b) constructed an elastic-to-plastic FEM for CFST ribs with a square or circular section. Tao et al. (2009; 2011), Hassanein (2010), and Ellobody and Young (2006a, b) carried out a nonlinear FEM on CFST short or long columns. Dai and Lam (2010) established a nonlinear FEM for the analysis of CFST columns with an elliptical section. Huang et al. (2010), and Hu and Su (2011) used ABAQUS to conduct nonlinear analysis on the behavior of CFST columns. Bijaya and Ren (2005) established a half-through arch bridge linear FEM by means of two-node beam elements using ANSYS.

The majority of the above analyses have focused on straight-welded or seamless small-diameter CFSTs, ignoring the influences of the concrete segregation, SWS strength, and gap composite defects on their bearing performance. However, actual CFSTs, particularly large-diameter CFST arch bridges that are in service in cold areas, will inevitably be affected by the above defects. Thus far, single-factor defects of CFST ribs have been studied by Liao et al. (2011, 2013), Han et al. (2016), Liu et al. (2013), Huang et al. (2017), and Schnabl and Planinc (2019). They performed a series of experiments and established FEMs for analytical investigations to estimate the circumferential gap, where the key calculating parameter was the section gap ratio (χ):

For a CFST rib with a circumferential gap, as illustrated in Fig. 5:

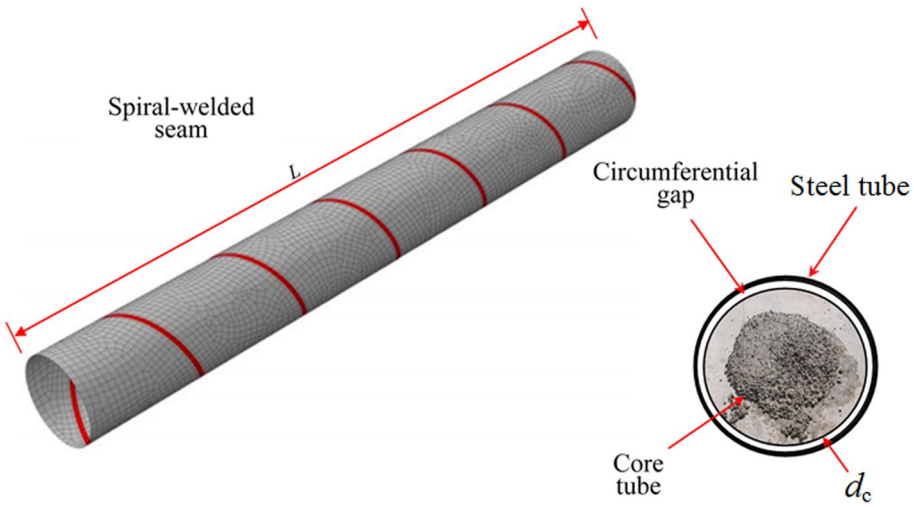

Fig. 5 Mesh of CFST composite defects

$$\chi=\frac{2\,d_c}{D}, \tag{1}$$

where d_c is the dimension of the circumferential gap and is designated as the maximum distance from the concrete core to the outer surface of the SWT, as indicated in Fig. 5; D is the outer diameter of the SWT section.

The circumferential gaps were produced in the rib of the CFST arch bridge, owing to concrete shrinkage and temperature gradient stresses during the service stage (Xie et al. 2019). However, thus far, no nonlinear FEMs on CFST arch ribs with circumferential gaps and decreased SWS strength composite defects have been presented.

This research aims to perform a series nonlinear FEM of a CFST arch bridge 6-m length rib element, which is the distance of the two bridge suspenders, with circumferential gap and SWS strength decreased composite defects under eccentric axial compression. The main aim of this research is as follows: First, a no-defect 3D elastic-to-plastic FEM is developed, in which only the nonlinear material constitutive model is included. Second, the bearing capacity of the CFST ribs with a single defect, namely the decreased SWS strength and circumferential gap, is studied. Third, a composite defect study is conducted, following which the ultimate strength of the CFST arch bridge rib is proposed.

2 FEM Analysis

2.1 General Conditions

The general finite element software (ABAQUS) was employed for the FEM. The SWT was simulated by 4-node reduced integration shell element (S4R). The spiral-weld seam was created using ABAQUS / CAE. First, the following settings were applied: "part" model, "set modeling space to 3D," "type to deformable," "shape in base feature to shell," and "type to revolution." Then, the sketch interface was entered, SWS was drawn in this interface, and spiral well seam was realized by setting the pitch value. The concrete core was modeled by 8-node hexahedral elements (C3D8), with three translation degrees of freedom (DoFs) at each node. A mesh optimization design was conducted to identify an appropriate mesh density for receiving reliable data. Figure 5 illustrates the 3D mesh of the CFST rib with composite defects.

Regarding this CFST arch bridge transverse brace, the thickness of the steel tube was only 10 mm, but the diameter was 720 mm, and the circumference was 2260 mm; therefore, the aspect ratio along the circumferential direction was 226. This means that if the ideal hexahedral solid element is used to discretize the steel tube, 226 units need to be arranged along the circumferential direction even if the roughest element is selected along the thickness direction, which would lead to data explosion, calculation difficulties, and low accuracy of results. If the length of the circular element is increased, the element stiffness matrix would be ill-conditioned for the case wherein the ratio of length to height is greater than 10. Moreover, the hourglass effect of the solid element would cause a large calculation error. Therefore, to improve the accuracy of the finite element simulation of the steel tube, the shell element was used in this study. To avoid the problem concerning compatibility of the degrees of freedom (DoFs) between the steel tube shell and concrete solid elements, this FEM established a column coordinate system for the steel tube in the post-processing stage.

We performed a mesh sensitivity analysis; the typical element length of 60 mm was considered for this FEM analysis, while the circumference of the steel tube was 2260 mm. Thereafter, 40 elements were arranged along the circumferential direction of the tube. Consequently, the center angle of each element was 9°. Within this angle range, the chord length was used to replace the arc length, which has little influence on the calculation results. Through the above analysis, the considered element length was determined to be technically reasonable.

Enforced displacement at the top reference point of a rib was applied to realize the eccentric axial loading boundary condition. As the bridge arch rib is a compression member with small eccentricity, the eccentricity was determined as $D/6$, according to the load combination. The rigid plate of the CFST ends was simulated by coupling the surface node DoFs on the reference points, which were located at the center of the upper and lower surfaces. All DoFs of one point were fixed, while a displacement of 0.025 L was applied to the other point, where L is the effective rib length.

2.2 Material Properties and Constitutive Models

2.2.1 Steel

The steel tube and concrete samples used in this FEM analysis were from the serviced arch rib of the Chang-Qing Hun River Bridge, as illustrated in Figs. 3 and 6.

Many stress (σ)–strain (ε) models have been used by different researchers for the steel tube, including the linear elastic perfectly plastic model (Roeder et al. 1999, Hu et al. 2003) with multi-curve hardening (Han et al. 2007). Steel exhibits less strain hardening at strains of general structural interest scope (ε<0.005). Very approximated axial stress–strain curves can be obtained by using different σ–ε models for steel. The FEM model developed in this study was used for the following simulation, unless otherwise specified. The mathematic model of the σ–ε relationship of a steel tube has little influence on the bearing capacity of rib and only affects the load–strain curve slightly at a post

Fig. 6 Steel tube specimen

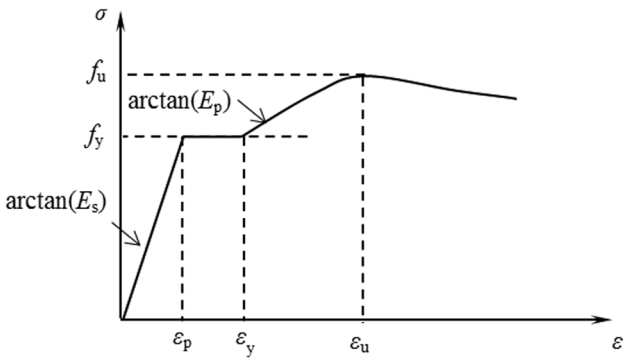

Fig. 7 Model for steel tube properties

point stage for the confined concrete core. However, the different σ–ε relationships of steel have a little influence on the load–strain curves of CFST rib at strains of interest in the arch bridge. Particularly for the arch bridge structure with a span of 150 m investigated in this study, a small strain will lead to changes in the bridge stiffness. A σ–ε model was proposed by Tao et al. (2013a, b) for steel tube with a validity strength ranging from 200 to 800 MPa. According to the tensile test of the steel tube specimen, the σ–ε relationship of the steel tube in this bridge arch rib obeys a trilinear material property model, as illustrated in Fig. 7.

This model was used to simulate the steel material in circular CFST ribs, which can be expressed as follows:

$$\sigma = \begin{cases} E_s \varepsilon & 0 \le \varepsilon < \varepsilon_y \\ f_y & \varepsilon_y \le \varepsilon < \varepsilon_p \\ f_u - (f_u - f_y) \cdot \left(\dfrac{\varepsilon_u - \varepsilon}{\varepsilon_u - \varepsilon_p} \right)^P & \varepsilon_p \le \varepsilon < \varepsilon_u \\ f_u & \varepsilon \ge \varepsilon_u \end{cases}, \tag{2}$$

in which E_s is the elastic modulus at the initial point of the σ–ε line; f_u is the ultimate strength of the steel tube in CFST arch rib for this case; ε_y is the yield strain, $\varepsilon_y = f_y / E_s$; ε_p is the strain at the site of strain hardening; ε_u is the ultimate strain corresponding to the ultimate strength, determined using Eqs. (3) and (4), respectively; and p is the strain-hardening exponent index calculated by Eq. (5).

$$\varepsilon_p = \begin{cases} 15\,\varepsilon_y & f_y \le 300 \text{ MPa} \\ [15 - 0.018(f_y - 300)]\,\varepsilon_y & 300 \text{ MPa} < f_y \le 800 \text{ MPa} \end{cases} \tag{3}$$

$$\varepsilon_u = \begin{cases} 100\,\varepsilon_y & f_y \le 300 \text{ MPa} \\ [100 - 0.15(f_y - 300)]\,\varepsilon_y & f_y < 300 \text{ MPa} \le 800 \text{ MPa} \end{cases} \tag{4}$$

$$P = E_p \cdot \left(\frac{\varepsilon_u - \varepsilon_P}{f_u - f_y} \right), \tag{5}$$

where E_p is the initial elasticity modulus at the point of strain hardening and is taken as 0.02 E_s. The following equation, proposed by Tao et al. (2013a, b) was used to distinguish f_u from f_y if there was no tensile failure experienced by the steel.

$$f_u = \begin{cases} \left(1.6 - 2 \times 10^{-3} \left(f_y - 200\right)\right) f_y & 200 \text{ MPa} \le f_y \le 400 \text{ MPa} \\ \left(1.2 - 3.75 \times 10^{-4} \left(f_y - 400\right)\right) f_y & 400 \text{ MPa} < f_y \le 800 \text{ MPa} \end{cases} \tag{6}$$

The parameters of the steel tube in this case are presented in Table 1.

As the steel tube was subjected to multiple direction stresses, a von Mises yield criterion F was employed to express the elastic limit in ABAQUS, which is defined as

$$F = \sqrt{3 J_2} = \frac{1}{\sqrt{2}} \sqrt{\left(\sigma_1 - \sigma_2\right)^2 + \left(\sigma_2 - \sigma_3\right)^2 + \left(\sigma_3 - \sigma_1\right)^2}, \tag{7}$$

Table 1 Parameters of steel tube

t	D	E_s	μ_s	f_y	f_u	ε_y	ε_u
mm	mm	MPa		MPa	MPa		
10	720	2.0 × 105	0.32	345	400	0.00192	0.179

t: thickness, D: outer diameter, μ_s: Poisson's ratio

where J_2 is the second stress invariant of the stress deviator tensor; and σ_1, σ_2, and σ_3 are principal stresses. The yield criterion of the steel tube was modeled by an associated flow rule.

When the stress points fall inside the yield surface, the steel tube behavior is linearly elastic. If the stresses of the steel tube reach the yield surface, the steel tube behavior becomes perfectly plastic. Consequently, the steel tube is assumed to fail and cannot resist any further loading.

2.2.2 Concrete

The Poisson's ratio μ_c, cylinder compressive strength f_c', and corresponding strain ε_c' of a concrete specimen with a diameter of 100 mm under uniaxial compressive stress are 0.21, 33 MPa, and 0.0033, respectively, in the case of this bridge.

The empirical Eq. (8) recommended in ACI318 (2011) was adopted to calculate E_c as 2.7×10^4 MPa, where f_c' is in MPa.

$$E_c = 4700\sqrt{f_c'} \tag{8}$$

Based on test data collected from Papanikolaou and Kappos (2007), the following equation was proposed to predict the ratio of f_{bc}/f_c' as 1.12:

$$f_{bc}/f_c' = 1.5\left(f_c'\right)^{-0.075}. \tag{9}$$

where f_{bc} is the initial equibiaxial compressive yield stress. When core concrete has to bear a circular confining pressure, the uniaxial compressive yield strength f_c' and corresponding strain ε_c' (Fig. 8) are substantially higher than those of unconfined concrete. The relations between f_{cc}' and f_c' and between ε_{cc}' and ε_c' were estimated by Mander (1988a, b).

According to Mander's model, Han (2016) established an equivalent σ–ε model to simulate the plastic behavior of the core concrete in CFSTs under compression:

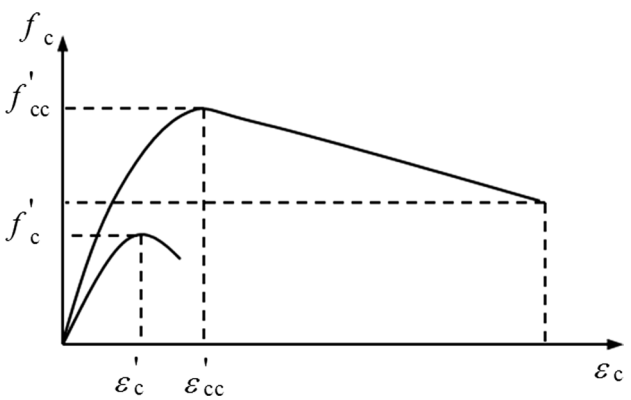

Fig. 8 Stress–strain curve

$$y = 2x - x^2 \tag{10}$$

$$y = \left\{ \begin{array}{ll} 1 + q\cdot\left(x^{0.1\xi} - 1\right) & (\xi \geq 1.12) \\ \frac{x}{\beta\cdot(x-1)^2 + x} & (\xi < 1.12) \end{array} \right\} (x > 1) \tag{11}$$

$$\sigma_0 = \left(1 + \left(-0.054\,\xi^2 + 0.4\xi\right)\left(\frac{24}{f_c'}\right)^{0.45}\right) f_c' \tag{12}$$

$$\varepsilon_0 = \varepsilon_{cc} + \left(1400 + 800\left(\frac{f_c'}{24} - 1\right)\right)\xi^{0.2} \tag{13}$$

$$q = \frac{\xi^{0.745}}{2 + \xi} \tag{14}$$

$$\beta = \left(2.36\times10^{-5}\right)^{(0.25+(\xi-0.5)^7)} f_c'^{2}\cdot 3.51\times10^{-4}, \tag{15}$$

in which $x = \varepsilon/\varepsilon_0$, $y = \sigma/\sigma_0$; the confinement factor ξ_c is expressed as

$$\xi = \frac{A_s f_y}{A_c f_c'}, \tag{16}$$

where A_s and A_c are the cross-sectional areas of the SWTs and core concrete, respectively.

The experimental data presented in (Liao et al. 2011) indicate that the core concrete of the CFST with a single defect of the circumferential gap was cracked when it reached the ultimate strength, without confinement from the outer SWTs. Therefore, the compressive σ–ε model proposed by Samani and Attard (2012) is used to describe unconfined concrete.

Once the ultimate bearing capacity of the rib element is attained, the cracked concrete tends to laterally expand, and the concrete begins to contact its outer SWT during the post point loading stage. At this time, interaction occurs between the outer SWTs and core concrete in the FEM, and the confinement capacity from the SWTs to the concrete is thus effective through the normal pressure stress (p) from then on.

Because the core concrete in the CFST arch bridge rib is usually subjected to multidirectional compressive stresses, the concrete destroyed is dominated by the compressive failure surface expanding with the increase in hydrostatic pressure. Hence, a linear Drucker–Prager yield criterion G (Fig. 9) is used to model the yield surface of the concrete, which is expressed as

$$G = q - p\tan\psi - d = 0, \tag{17}$$

where

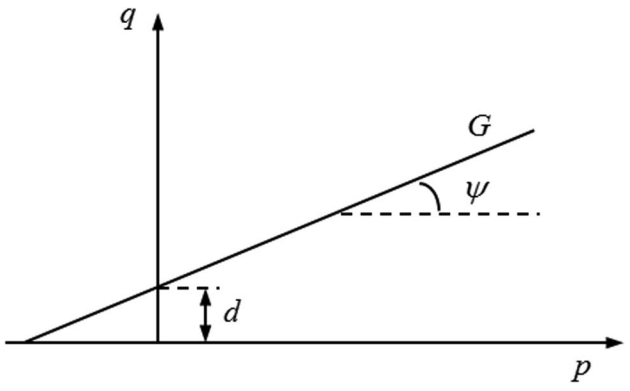

Fig. 9 Drucker–Prager criterion

$$p = -\left(\sigma_1 + \sigma_2 + \sigma_3\right)/3 \tag{18}$$

$$d = \left(1 - \frac{\tan\psi}{3}\right) f_{cc}^{'} \tag{19}$$

$$q = \frac{\sqrt{3J_2}}{2}\left[1 + \frac{1}{K} - \left(1 - \frac{1}{K}\right)\left(\frac{r}{\sqrt{3J_2}}\right)^3\right] \tag{20}$$

$$r = \left[\frac{9}{2}\left(S_1^3 + S_2^3 + S_3^3\right)\right]^{1/3}, \tag{21}$$

in which S_1, S_2, and S_3 are the primary stress deviators. The ratio of the second stress invariant on the tensile meridian to that on the compressive meridian K is the key parameter used to determine the yield surface of the concrete plasticity stress space. According to Yu et al. (2010a; b) and Tao et al. (2013a, b), Eq. (22) can be deduced to determine K as 0.846 in this study:

$$K = \frac{5.5}{5 + 2\left(f_c^{\prime}\right)^{0.075}}. \tag{22}$$

Moreover, β represents the material parameters determined from experimental data, and $\beta = 20°$ is used (Ellobody and Young 2006a, b). According to the deep analysis of the CFST FEM (Tao et al. 2013a, b), the following equation is suggested:

$$\psi = \begin{cases} 56.3(1-\xi) \\ 6.672\, e^{\frac{7.4}{4.64+\xi}} \end{cases}. \tag{23}$$

Therefore, $\xi = 0.42$ in this CFST bridge arch rib, and $\beta = 33°$.

2.2.3 SWTs–Core Concrete Interface

In the past twenty years, a normal direction hard contact interaction pressure model and a tangential direction friction Coulomb model for the surface between the SWTs and core concrete have been widely used in the FEM of CFST columns (Han et al. 2007), by ABAQUS software. These types of models were also used in this study. For the CFST with a circumferential gap or not, the shear stress (τ_{crit}) on the interface between the core concrete and SWT will continue to increase with an increase in the normal contact interaction until it exceeds the surface bond strength (τ_{bond}). Thereafter, a relative slip is constructed and the shear stress in taken as a constant value. The τ_{crit} value is expressed as follows:

$$\tau_{crit} = u \cdot p \geq \tau_{bond}, \tag{24}$$

where u is the friction coefficient, which is taken as 0.6 in this case (Wang et al. 2013), and

$$\tau_{bond} = 2.314 - 0.0195 \cdot (D/t). \tag{25}$$

The surface of the core concrete in a CFST rib with a circumferential gap is not in direct contact with the inner surface of the SWTs during the initial bearing stage. Therefore, both the tangential shear stress and normal contact pressure stress are initially taken as zero in this FEM. Then, after contact occurs, the tangential frictional stress (τ_{fric}) relies on the value of the normal pressure stress (p_n) and can be expressed as:

$$\tau_{fric} = u \cdot p_n. \tag{26}$$

3 Verification of FEM

A comparison between the experimental data of Gunawardena and Aslani (2018), Gunawardena et al. (2019), Liao et al. (2011, 2013), and the FEM analysis results, was carried out to verify the FEM rationality of this bridge rib. It can be observed that the ribs with decreased SWS strength or a single defect of a circumferential gap generally exhibited outward local buckling for the steel tubes at the SWS, while the overall lateral deflection at mid-height was also observed. The predicted distorted modes scientifically demonstrated reasonable agreement with the experienced phenomenon, despite little differences in terms of the local buckling position. The predicted eccentric axial load (N) versus axial strain (ε) curves were compared with the typical measured curves. The predicted ultimate limit states were compared with those obtained from tests. In brief, obtained identical agreement was obtained between the predicted FEM and experimental data.

For a CFST rib with a circumferential gap, it appears that the point when the core concrete interacts with the SWTs is a decisive factor affecting the rib bearing capacity. There has been no SWS strength defect research thus far, and the SWSs studied by Gunawardena and Aslani (2018), Gunawardena et al. (2019) were standard welds that met the design requirements and had no defects. However, the arch rib element SWSs of this bridge are defective. Therefore, the composite defects of the CFST columns with a decreased SWS strength and circumferential gap are analyzed in the following sections.

The presented FEM analysis is valid for a CFST arch rib of an actual bridge as the circumferential gap runs through the entire steel tube according to the FEM. Because the minimal span of the whole bridge is 120 m and the length of the finite element analysis unit is 6 m, it can be assumed that χ in the 6-m long member is a fixed value. As part of this analysis, four groups of different χ values were employed, which can cover the range of χ values that may be presented in the tube. Therefore, SWS geometric imperfections are not analyzed separately; however, the influence of these geometric imperfections is replaced by the stress state of small eccentric compression. In addition, as per existing literature, it has been determined that the instability mode and load-bearing characteristics of spiral-welded stainless steel tubes are significantly different from those of this CFST; therefore, these can be studied in the feature.

3.1 Analysis of CFST Rib with or Without SWS Defect

The typical CFST stub arch elements selected herein to conduct behavior analysis generally have the same parameters as those of the Chang-Qing Hun River Bridge. The analytical columns have a sectional dimension of $D \times t = 720 \times 10$ mm, and concrete strength of $f_c' = 41$ MPa as the theoretical strength of the bridge design; however, because of the discrepancy regarding the concrete strength inside the steel tube, the strength of the core column is corrected according to the area ratio with reference to the unconfined compressive strength test, and a strength value of 33 MPa is employed instead. The steel parameters are listed in Table 1.

3.1.1 *N-ε* Curves of CFST Rib with or Without SWS Defect

The SWS strength (S) was 50%, 70%, and 100%, respectively, of an ideal strength as strong as the parent material. The screw pitch was 0.95 m, and the length L was 6000 mm. To analyze the influence of the SWS-S on CFST bearing capacity, the empty steel tube (EST) was firstly analyzed, following which the CFST truss element was analyzed, as illustrated in Fig. 10, which compares the N–ε curves of the EST with and without an SWS defect. It can be observed from Fig. 10a that the N of the EST without an SWS defect exhibited a strain-hardening capacity until a large axial strain ($\varepsilon = 0.03$) was achieved, after the yield strength was reached. However, the 30% and 50% strength decreases caused an EST strength loss of 5.8% and 29.2%, respectively, owing to the SWS defects, which also resulted in a loss of the strain-hardening capacity. Therefore, it can be understood that the strength reduction of the EST with an SWS defect was mainly owing to the decreased strength contribution.

It can be observed from Fig. 10b that the N versus ε curves of the CFST truss element almost coincided with one another under different SWS defect conditions. Therefore, it can be concluded that the strength reduction of the EST with an SWS defect had almost no effect on the CFST bearing capacity when the internal concrete had no defects.

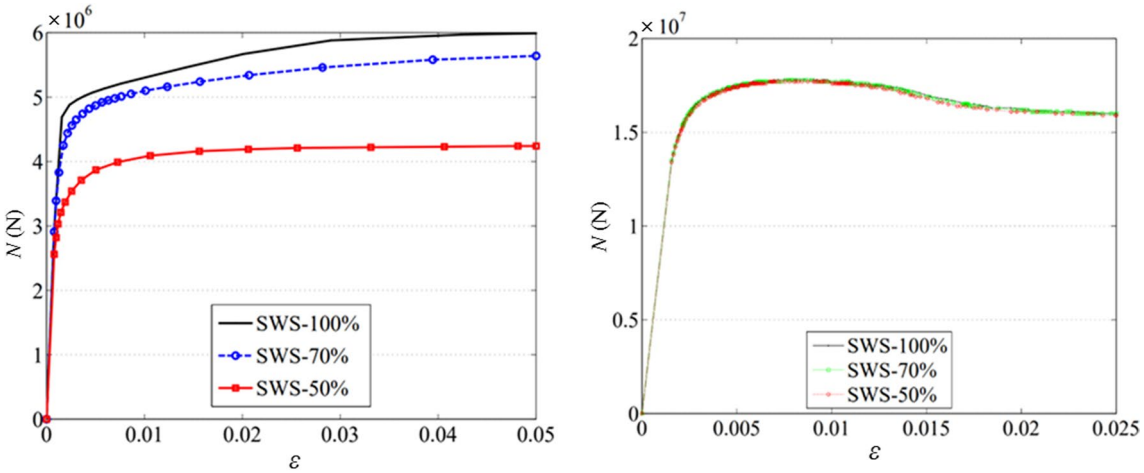

(a) EST **(b)** CFST

Fig. 10 Comparison of N versus ε relations

Because the defect regarding SWS in this bridge is spiral in nature, which is different from the longitudinal crack defect, it maintains a part of the constraint in the circumferential direction and does not completely lose the constraint ability; therefore, its influence on the strength of the components is limited. In this case, the confining coefficient $\xi = \frac{A_s f_y}{A_c f_c} = 0.42$ is relatively high, which shows the limited effects of SWS defects on composite-form parts. However, different CFSTs need to be analyzed in detail, and similar conclusions cannot be drawn. This is certificated by the observations of previous experiences (Gunawardena and Aslani 2018; Gunawardena et al. 2019).

3.1.2 Typical Destroyed Modes With or Without SWS Defect

The typical destroyed modes of the EST rib are compared in Fig. 11, in which the deformations have been amplified to illustrate the deformed shapes of the ribs. Local fold-shaped buckling of the SWSs was found on the compression side of the EST when the SWS-*S* was less than that of the parent material, and this phenomenon became increasingly obvious with the decrease in the SWS-S.

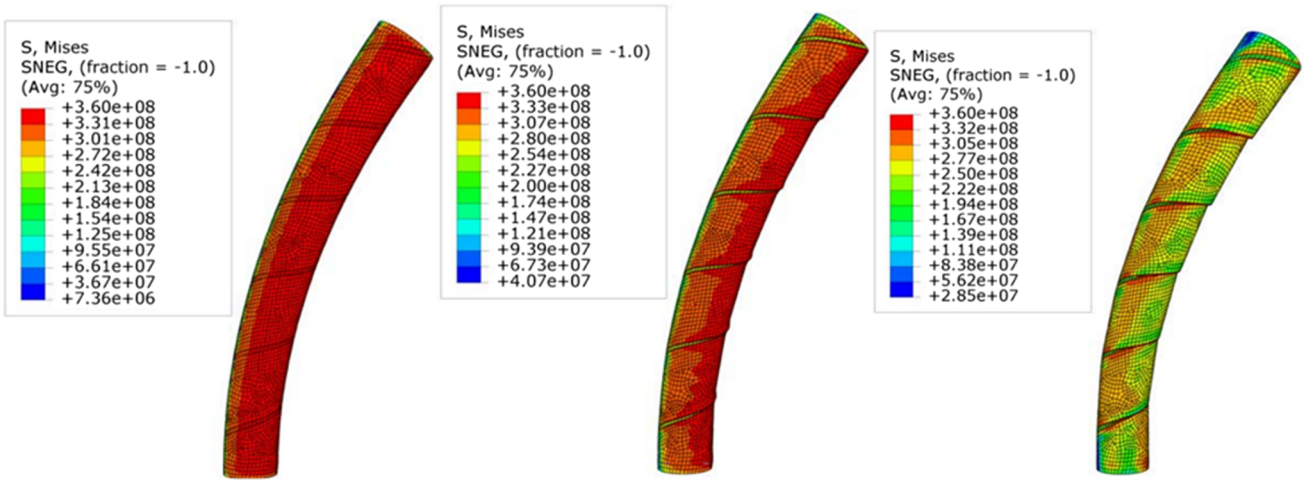

(a) SWS: 100% **(b)** SWS: 70% **(c)** SWS: 50%

Fig. 11 EST Mises stresses with different SWS-*S*

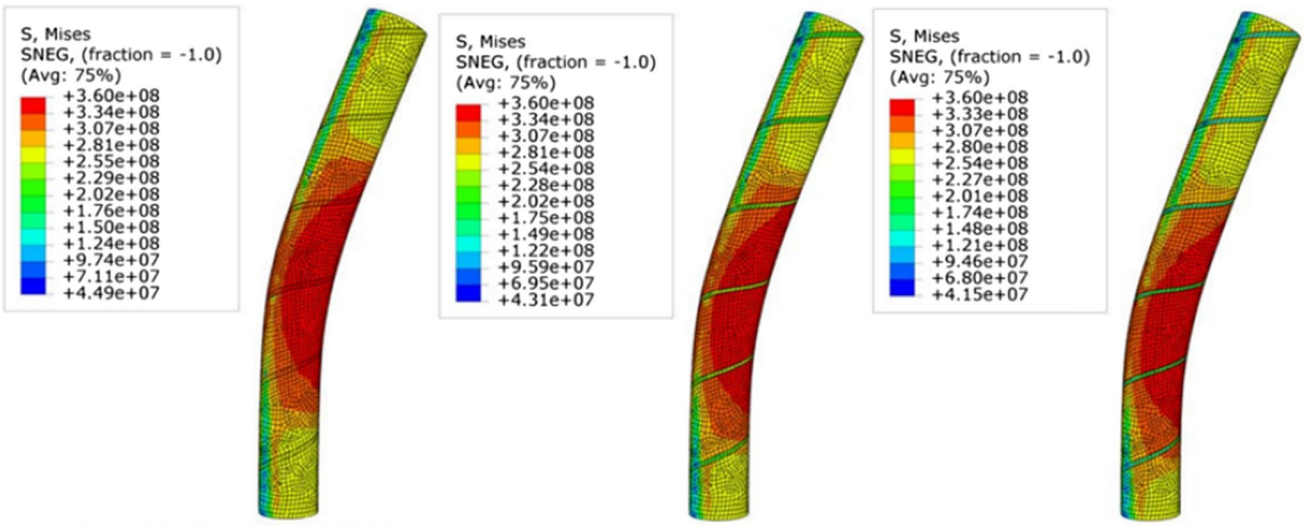

(a) Tube SWS: 100% **(b)** TubeSWS: 70% **(c)** Tube SWS: 50%

Fig. 12 Tube Mises stresses in CFST with different SWS-*S*

The typical SWT failure modes in the CFST truss elements are compared in Fig. 12, where the deformations have been amplified to illustrate the deformed rib shapes.

Figure 12 illustrates that the strength of the outer SWTs of the CFST decreased at the weld seam; however, it was not similar to the EST failure modes with local fold buckling. Moreover, a strong capability of confining the core concrete was demonstrated, which provided full support for the outer steel tube and prevented local bucking if there were no defects in the core concrete. This ensured the coinciding performance of the steel tube and concrete working together.

Figure 13 presents the Mises stresses of the core concrete of the CFST under different SWS-*S*. It was found that the stresses (Mises) carried by the SWTs or core concrete and the CFST deformation were approximately the same for the rib with and without an SWS-S defect. This occurred despite the SWS causing a strength loss of the SWTs belt of 30% to 50% in this example owing to the weld seam defects.

Therefore, it can be realized that the CFST rib strength reduction with an SWS-S defect was not obvious when the core concrete was fully filled. It can also be determined that the strength of the SWS with defects was decreased at the weld area.

3.2 3. 2. Analysis of CFST Arch Rib with Through-Type Circumferential Gap Defect

3.2.1 *N–ε* Curves with Through-Type Circumferential Gap Defect

Figure 14 compares the $N-\varepsilon$ curves of the CFST ribs with a through-type circumferential gap ($\chi = 1.4\%$, 2.8%, and 4.2%) or without. It can be observed from Fig. 14a that the CFST exhibited typical strain-hardening characteristics when there were no circumferential gaps, which is consistent with the results in Gunawardena and Aslani (2018), Gunawardena et al. (2019).

The strain softening and yield occurred when circumferential gaps existed in the CFST rib, which is consistent with the results of Liao et al. (2013), Han (2016), and Liu et al. (2013). For clarity of the analysis, a group of key points were marked on the $N-\varepsilon$ curves, as indicated in Fig. 14. Points A_0 to A_3 correspond to the strain when the peak load was attained. It can be observed from Fig. 14a that the *N* of the rib with the circumferential gaps decreased suddenly after the peak load; however, the *N*–*ε* curves of the rib without circumferential gap defects exhibited strain hardening. Thereafter, when the core concrete is in contact with the outer SWTs, the *N* increased again (Point B). To analyze the influence of the gap distances on the CFST bearing capacity more clearly, the *N*–*ε* curves under the conditions of each gap are presented separately in Fig. 14b. The *N*–*ε* curves of the rib with the 1.4% circumferential gap were smooth. However, at Points B_2 and B_3, the *N*–*ε* curves of the rib with

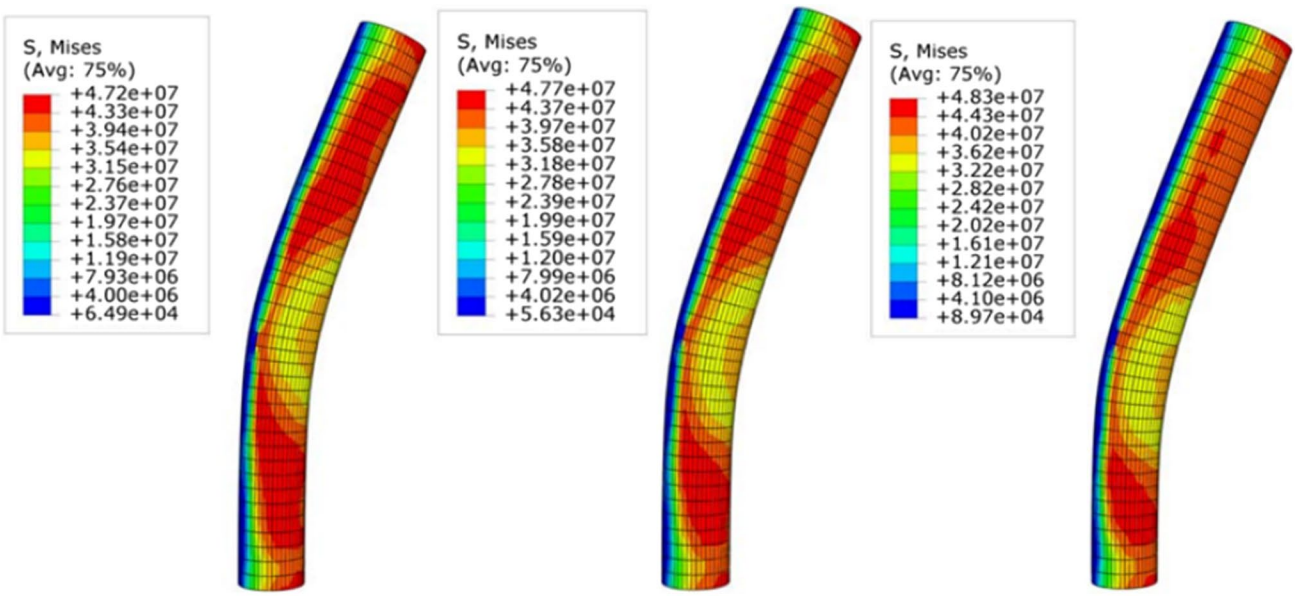

(a) ConcreteSWS:100% **(b)** ConcreteSWS:70% **(c)** ConcreteSWS:50%

Fig. 13 Concrete Mises stresses in CFST with different SWS-*S*

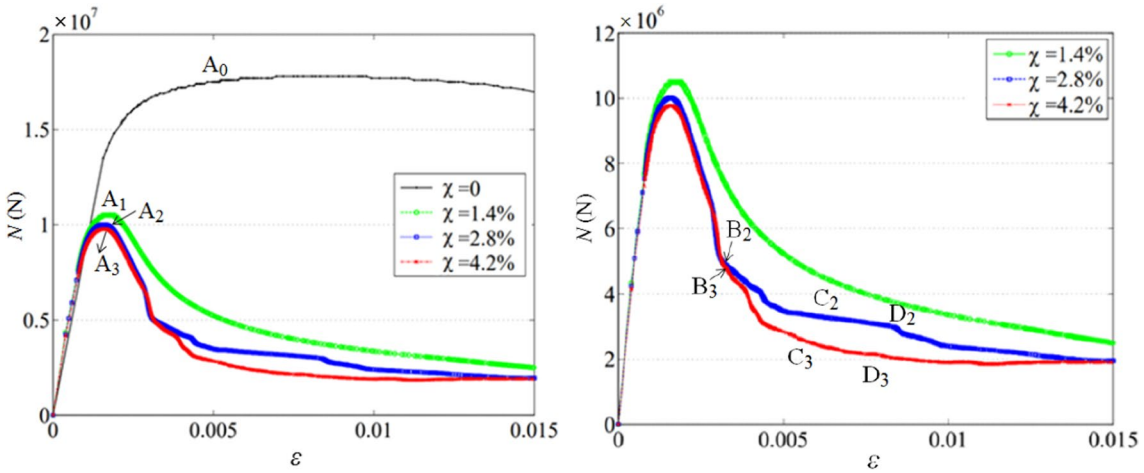

(a) With or without gaps **(b)** With different circumferential gaps

Fig. 14 Comparison of N versus ε relations

the 2.8% and 4.2% circumferential gaps, respectively, began to increase again. Points C_2 and C_3 refer to the case at which the ε yield stopped, and thereafter, points D_2 and D_3 refer to the strain softening again.

3.2.2 Typical Destroyed Modes with Through-Type Circumferential Gap Defect

The typical destroyed modes of the CFST rib are compared in Fig. 15, and the elephant foot-shaped buckling deformation is amplified two times to illustrate the deformed shapes of the columns more clearly. These were found near the bottom of the CFST stub column. It is worth noting that, for the CFST with $\chi = 1.4\%$, only one elephant foot-shaped buckling deformation occurred, while for the CFST with $\chi = 2.8\%$ and 4.2%, there were two, indicating that a larger gap resulted in a larger space for local buckling deformation of the steel tube.

The deformed shapes of the concrete at different times are presented in Fig. 15. It can be observed that the concrete

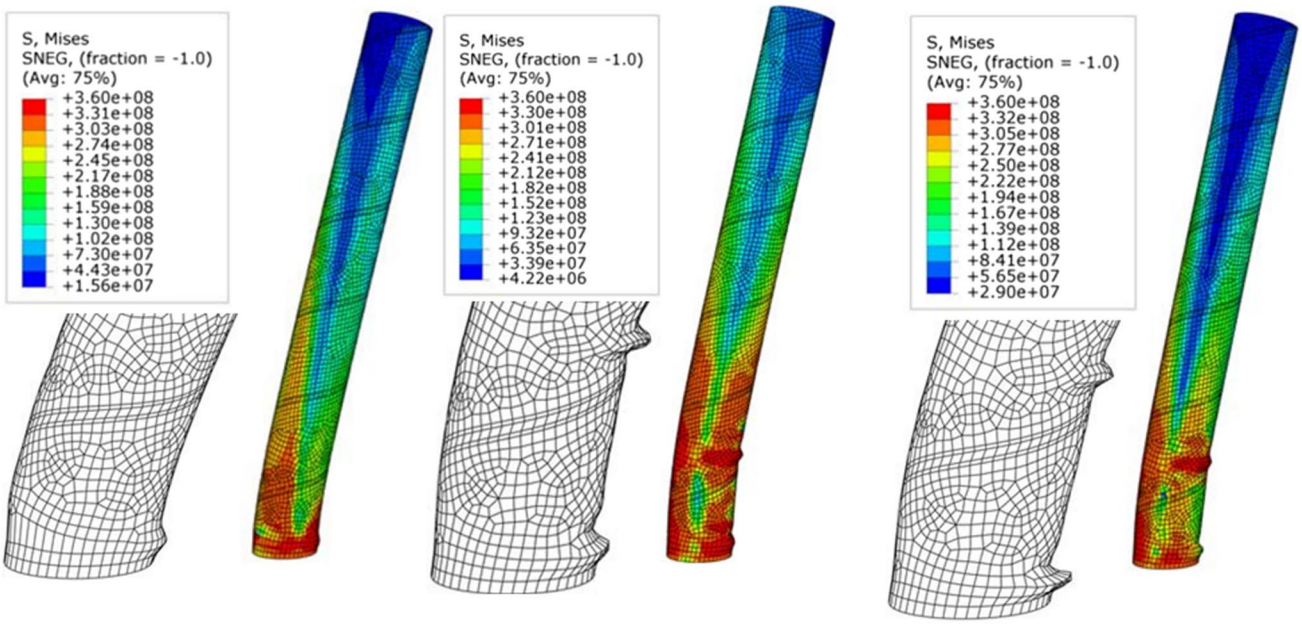

(a) χ= 1.4% **(b)** χ= 2.8% **(c)** χ= 4.2%

Fig. 15 Concrete Mises stresses in CFST with different SWS-*S*

exhibited different bending deformation modes under different circumferential gap depths.

When the depth level was low, the concrete bending deformation was closer to that under a complete constraint, as indicated in Fig. 16.

With the increase in the circumferential gap depth, the bending deformation and stress became increasingly concentrated at the root, and the CFST exhibited the situation of local fracture and the brittle failure stage. It can be discovered that, before the core concrete interacted the outer SWTs, the greatest cross section deformation of the concrete occurred at the root. Then, after the core concrete made contact with the outer SWTs, the cross section deformation of the concrete at the root was confined by the SWTs. As a result, the cracked location of the concrete tended to move towards the rib mid-height. Failure of the concrete was observed at the sections where the SWTs local buckling occurred, as indicated in Fig. 15.

3.3 Analysis of CFST Rib with SWS-S and Circumferential Gap Composite Defects

3.3.1 χ –N–ε Curves with SWS-S and Circumferential Gap Composite Defects

Figure 17 compares the χ–$N-\varepsilon$ curves of the CFSTs with a through-type circumferential gap ($\chi = 1.4\%$, 2.8%, and 4.2%) in three and two dimensions.

It can be observed from Fig. 17a that all of the CFST truss elements exhibited typical smooth strain-softening characteristics when circumferential gaps existed without SWS strength defects, which is consistent with the results of Gunawardena and Aslani (2018), Gunawardena et al. (2019). The stress yield steps occurred when there were circumferential gaps in the CFST, which is consistent with the results of Liao et al. (2011, 2013), Han (2016), and Liu et al. (2013). This is quite similar to the results presented in Fig. 14b. However, under the composite effects of different SWS strength levels, the N–ε curves of each component exhibited different variation rules. With the decrease in SWS strength, the number and length of the yield steps on the N–ε loss curve increased gradually, indicating that the N–ε loss curve of the weld seam strength on the CFST increased gradually after the peak strength. This was mainly owing to the weakened restraint ability of the local steel tube on the concrete at the SWS, which reduced the composite bearing capacity of the CFST.

3.3.2 Typical Destroyed Modes with SWS-S and Circumferential Gap Composite Defects

The typical failure modes of the CFST stub columns are compared in Figs. 18 and 19 under different SWS defects, where the elephant foot-shaped buckling deformation is amplified two times to illustrate the deformed shapes of the columns more clearly. These were found near the bottom of the CFST stub column. It is worth noting that, for the

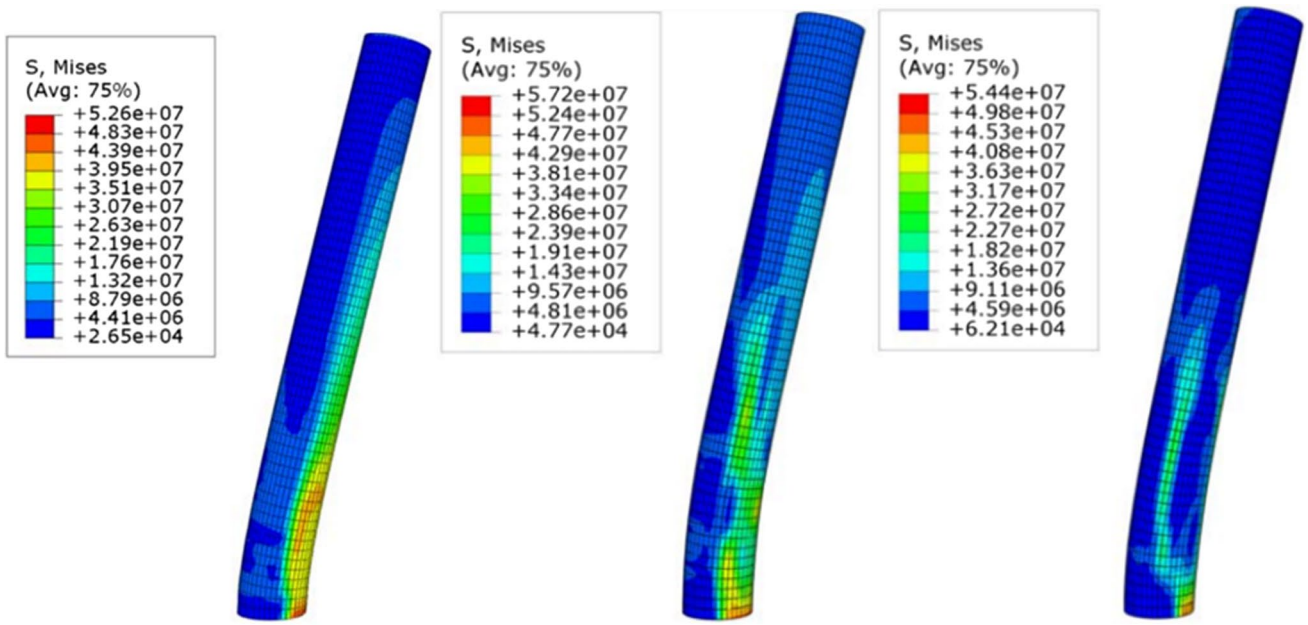

(a) χ = 1.4% **(b)** χ = 2.8% **(c)** χ = 4.2%

Fig. 16 Concrete Mises stresses in CFST with different circumferential gap depths

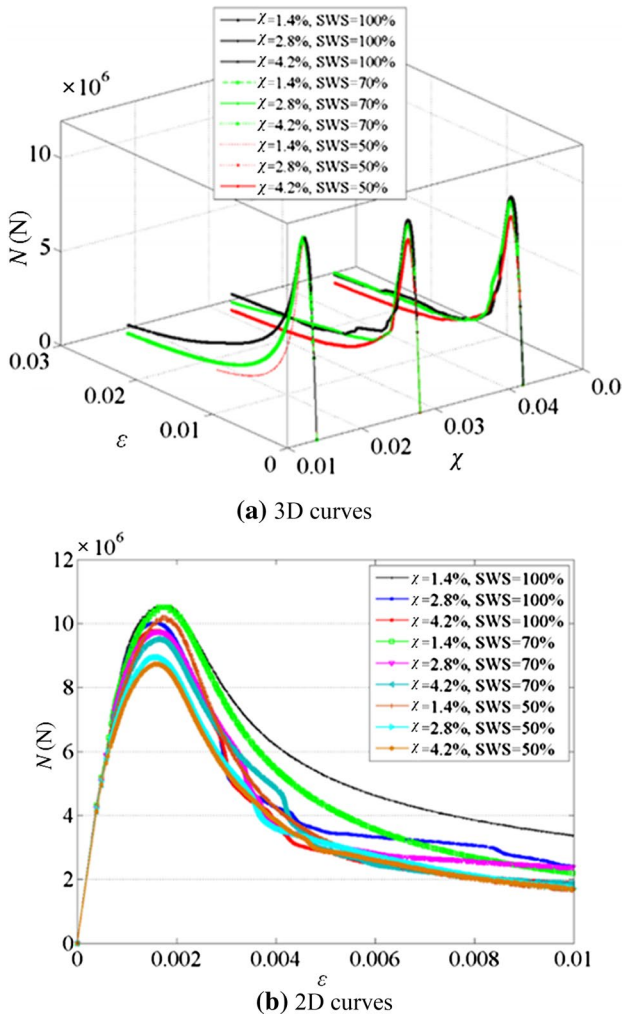

Fig. 17 χ–N–ε– curves

CFST with $\chi = 1.4\%$, only one elephant foot-shaped buckling deformation occurred, while for the CFST with $\chi = 2.8\%$ and 4.2%, there were two, the same as in Fig. 16. However, as opposed to the state when the SWS was intact, the location and shape of the local buckling of these steel tubes differed. When the SWS was defective, the tensile yield position of the steel tubes appeared at the first welding seam, although the χ differed. In addition to the first weld line, the compressive yield also appeared at the foot of the compressive side with the increase in χ.

As illustrated in Fig. 18, when the SWS strength was 70% of the ideal strength, and χ increased three times from 1.4 to 4.2%, the tensile yield of the first SWS of the CFST root on the tensile side followed the rotation direction of the SWS and transferred to the folded failure of the compression side, indicating that the SWS defects were the source of the CFST bending failure.

Figure 19 illustrates that, when the SWS strength decreased to 50% of the ideal strength of the steel tube, with χ increasing from 1.4 to 4.2%, the tensile yield of the first SWS of the CFST root on the tensile side followed the rotation direction of the SWS and transferred to the compression side. However, local compressive failure similar to that in Fig. 18 did not occur on the compressive side, indicating that the degree of the weld defect had an important influence on the local yield failure mode of the CFST. The stress and deformation of the core concrete column were basically consistent with the results in Fig. 16; however, we do not provide further details here.

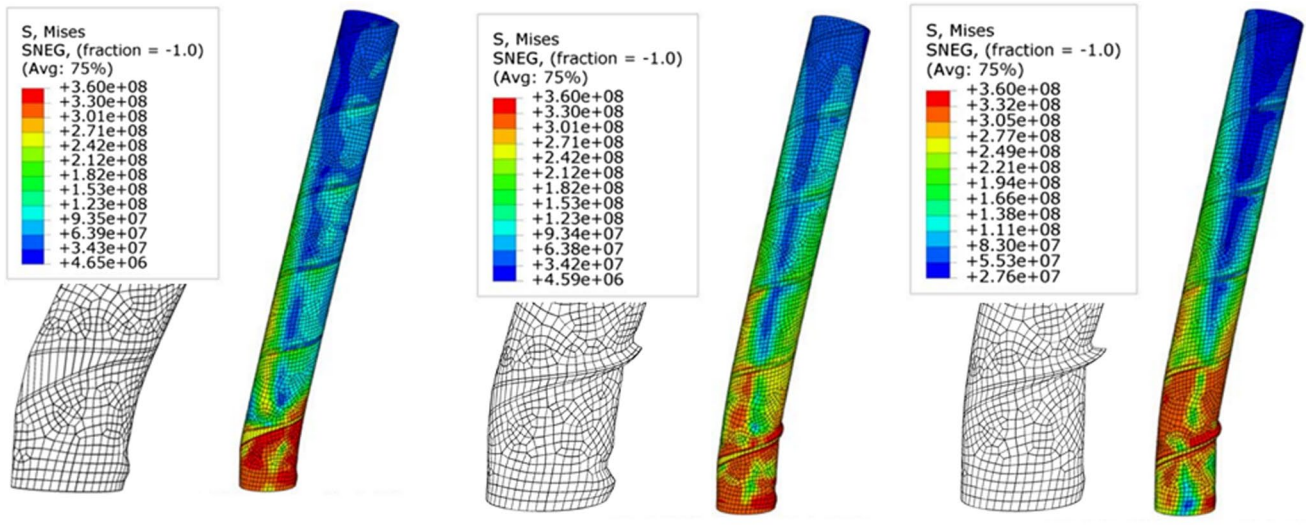

(a) χ = 1.4% (b) χ = 2.8% (c) χ = 4.2%

Fig. 18 Concrete Mises stresses in CFST with 70% SWS-*S*

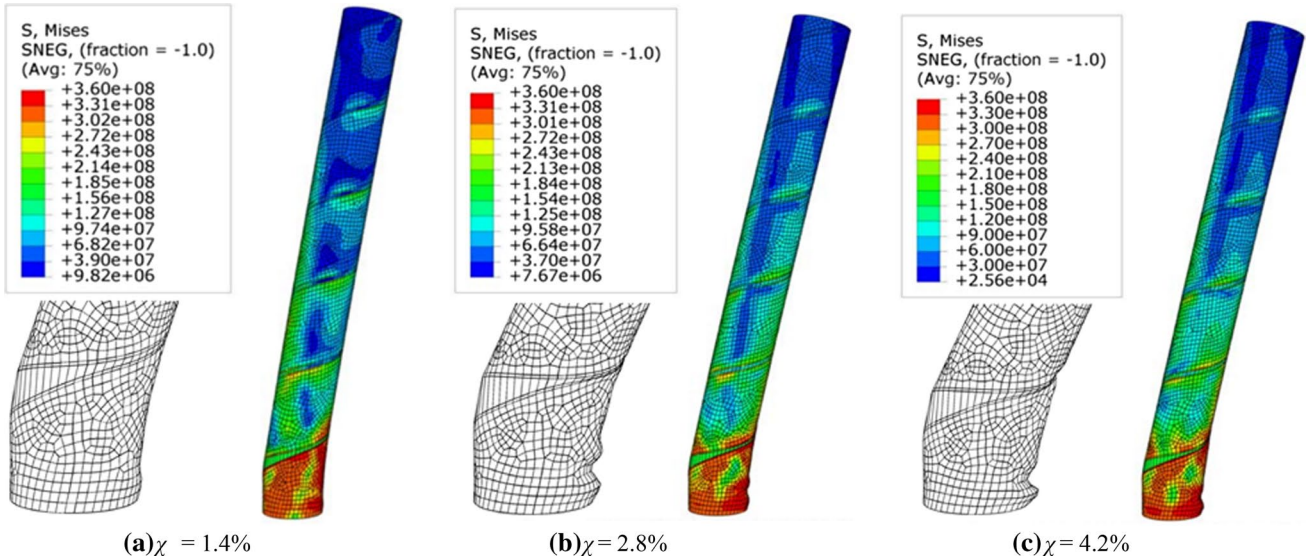

(a) χ = 1.4% **(b)** χ = 2.8% **(c)** χ = 4.2%

Fig. 19 Concrete Mises stresses in CFST with 50% SWS-*S*

4 Composite Strength Index

For quantitative evaluation of the influence of the SWS strength and circumferential gap composite defects on the CFST bearing capacity, a strength index SI is defined, as follows:

$$\mathrm{SI} = \frac{N_{\mathrm{c-def}}}{N_{\mathrm{n-def}}}, \tag{27}$$

where $N_{\mathrm{c-def}}$ is the maximum value of the CFST rib *N*–*ε*– curves with composite defects, and $N_{\mathrm{n-def}}$ is the maximum value of the CFST rib *N*–*ε*– curves without defects. The values matrix of *SI* for the CFST truss elements with different composite defects is presented in Fig. 20. According to experience data reported by Liao (Kaizhong et al. 2019), if χ is reduced to 0.05%, the strength loss of the CFST rib is less than 5%. When the *SI* of the CFST does not consider the reduction in the SWS strength, it is close to the results of Hassanein (2010), Ellobody and Young (2006a, b), and Dai and Lam (2010), but the actual χ of this bridge was much higher than the above experimental level, so the coverage area of the FEM calculated results was larger. The *SI* values also decreased rapidly from 1 to 0.5899 when χ increased from 0 to 0.014. However, when χ increased further from 0.014 to 0.042, *SI* did not decline rapidly, but decreased from 0.589 to 0.549. This pattern of the rapid *SI* decline also occurred when the SWS intensity was 0.5 to 0.7. When the SWS strength was equal to 0.7 and 0.5, the χ value increased from 0 to 0.042, and the *SI* value decreased from 1 to 0.5337 and 0.4899, respectively. Therefore, a multiple linear regression method was adopted to establish the

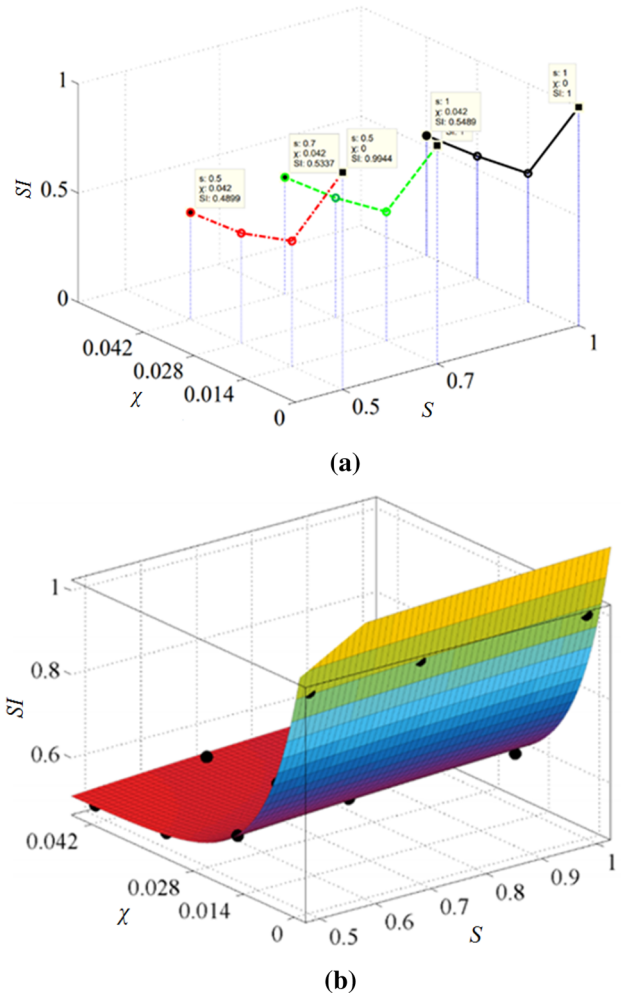

Fig. 20 Influence of χ and *S* on *SI*

relationship between SI and χ, and S, as follows (illustrated in Fig. 20):

$$SI = a\,e^{-b\chi} + (1-a)\,s^{c}\,. \tag{28}$$

The coefficients (with 95% confidence bounds) were as follows: $a = 0.4616(0.4407, 0.4825)$, $b = 144$ (113.7, 174.4), and $c = 0.07725$ (0.01871, 0.1358). The goodness of fit was determined as follows: SSE: 0.001316, R-square: 0.9959, adjusted R-square: 0.995, and RMSE: 0.01209. It can be determined from Eq. (28) that the significance of χ on SI was substantially higher than that of S. Furthermore, the circumferential gap had a significant effect on the destroyed mode, bearing capacity, and corresponding deformation of the CFST ribs.

5 Conclusions

In this study, ultrasonic scanning experimental field data of the Chang-Qing Hun River Bridge were collected and were used to develop a composite FEM for simulating the CFST arch bridge rib under eccentric axial compression. This calculated model was compared with existing FEM developed by Liao et al. (2013), Han (2016), and Tao et al. (2013a, b), in terms of prediction accuracy. The following conclusions can be drawn based on this study:

(1) The FEMs and experiments of Liao et al., Han et al., and Tao, among others, provide reasonable predictions for a normal, small χ or only SWS strength defect, respectively, of CFST columns; however, these underestimate the significant effect of χ on the ultimate strengths of circular truss element ribs for the CFST during long service in harsh conditions in the arch bridge practice.

(2) A group of FEMs was developed in this study for the CFST truss rib of the arch bridge, where the composite defects of the steel tube SWS strength and circumferential gap between the core concrete column and outer SWTs were calibrated against field ultrasonic inspection test data. Meanwhile, the strain hardening/softening and yielding laws of the peak-post curves of the CFST for steel tube local buckling coupled with different depths of χ were obtained.

(3) A new strength index, SI, of the CFST under composite defects was defined on the group of FEM results. The predictions using the new index were compared with the test data collected, which indicated that the new index is more accurate and versatile in calculating CFST ribs with composite defects. The new index SI expression quantitatively illustrates that χ has a more significant impact on the CFST bearing capacity than SWS-S, and therefore, reducing the circumferential gap is a key index for ensuring the CFST arch bridge bearing capacity.

Funding This research was supported by the National Key Research and Development Program of China (No. 2018YFD1100404), Province Natural Science Foundation of Liaoning, China (No. 20180550442), Plan of Liaoning Province to revitalize Liaoning talents (No. XLYC1907121), and Scientific Research Project of Liaoning Provincial Department of Education (No. lnjc201904).

Compliance with Ethical Standards

Conflict of interest The authors declare no conflict of interest.

References

American Concrete Institute (2011) Building code requirements for structural concrete (ACI 318–11) and commentary. Farmington Hills, MI, USA

Bijaya J, Ren WX (2005) Structural finite element model updating using ambient vibration test results. J Struct Eng 131:617–628

Chen H, Xu B, Mo Y, Zhou T (2018) Multi-scale stress wave simulation for aggregates segregation detection of concrete core in circular CFST coupled with PZT patches. Materials 11:1223–1240

Dai X, Lam D (2010) Numerical modelling of the axial compressive behaviour of short concrete-filled elliptical steel columns. J Constr Steel Res 66:931–942

Ding QJ, Hu SG, Guan B (2001) Application of large-diameter and long-span micro-expansive pumping concrete filled steel tube arch bridge. J Wuhan Univ Technol-Mater Sci 1:11–15

Dong W, Wua Z, Zhou X, Tan Y (2016) Experimental studies on void detection in concrete-filled steel tubes using ultrasound. Constr Build Mater 128:154–162

Ellobody E, Young B (2006a) Nonlinear analysis of concrete-filled steel SHS and RHS columns. Thin-Walled Struct 44:919–930

Ellobody E, Young B (2006b) Design and behaviour of concrete-filled cold-formed stainless steel tube columns. Eng Struct 28:716–728

Gunawardena Y, Aslani F (2018) Behaviour and design of concrete-filled mild-steel spiral welded tube short columns under eccentric axial compression loading. J Constr Steel Res 151:146–173

Gunawardena Y, Aslani F, Uyc B (2019) Behaviour and design of concrete-filled mild-steel spiral welded tube long columns under eccentric axial compression loading. J Constr Steel Res 159:341–363

Han LH (2016) Concrete filled steel tubular structures, 3rd edn. China Science Press, Beijing **[in Chinese]**

Han LH, Yao GH, Tao Z (2007) Performance of concrete-filled thin-walled steel tubes under pure torsion. Thin-Walled Struct 45:24–36

Han LH, Ye Y, Liao FY (2016) Effects of core concrete initial imperfection on performance of eccentrically loaded CFST columns. J Struct Eng 142:04016132-1–04016132-13

Hassanein MF (2010) Numerical modeling of concrete-filled lean duplex slender stainless steel tubular stub columns. J Constr Steel Res 66:1057–1068

Hu HT, Su FC (2011) Nonlinear analysis of short concrete-filled double skin tube columns subjected to axial compressive forces. Mar Struct 24:319–337

Hu HT, Huang CS, Wu MH, Wu YM (2003) Nonlinear analysis of axially loaded concrete-filled tube columns with confinement effect. J Struct Eng 129:1322–1329

Huang H, Han LH, Tao Z, Zhao XL (2010) Analytical behaviour of concrete-filled double skin steel tubular (CFDST) stub columns. J Constr Steel Res 66:542–555

Huang YH, Liu AR, Fu JY, Pi YL (2017) Experimental investigation of the flexural behavior of CFST trusses with interfacial imperfection. J Construct Steel Res 137:52–65

Liao FY, Han LH, He SH (2011) Behavior of CFST short column and beam with initial concrete imperfection: Experiments. J Constr Steel Res 67:1922–1935

Liao FY, Han LH, Tao Z (2013) Behavior of CFST stub columns with initial concrete imperfection: analysis and calculations. Thin-Walled Struct 70:57–69

Liu XP, Sun Z, Tang S, Huang HY, Liu AR (2013) A new calculation method for axial load capacity of separated concrete-filled steel tubes based on limit equilibrium theory. J Cent South Univ 20:1750–1758

Liu H, Xia H, Zhuang M, Long Z, Liu C, Cui J, Xu B, Hu Q, Liu QH (2019) Reverse time migration of acoustic waves for imaging based defects detection for concrete and CFST structures. Mech Syst Sign Process 117:210–220

Mander JB, Priestley MJN, Park R (1988a) Theoretical stress-strain model for confined concrete. J Struct Eng 114:1804–1826

Mander JB, Priestley MJN, Park R (1988b) Observed stress-strain behavior of confined concrete. J Struct Eng 114:1827–1849

Pan S, Zhu Y, Li D, Mao J (2018) Interface separation detection of concrete-filled steel tube using a distributed temperature measuring system. Appl Sci 8:1653–1672

Papanikolaou VK, Kappos AJ (2007) Confinement-sensitive plasticity constitutive model for concrete in triaxial compression. Int J Solids Struct 44:7021–7048

Peng G, Nakamura S, Zhu X, Wu Q, Wang H (2017) An experimental and numerical study on temperature gradient and thermal stress of CFST truss girders under solar radiation. Comput Concr 20:605–616

Pham DD, Nguyen PC (2019) Finite element modelling for axially loaded concrete-filled steel circular tubes. In: Proceedings of the 5th international conference on geotechnics, civil engineering works and structures, 54:75–80

Pham DD, Nguyen PC, Le HA (2019) Normal and high strength concrete-filled steel box columns under axial compression. In: Proceedings of the 17th international symposium on tubular structures, ISTS2019, 32:80–85

Ramge P, Proske T, Kühne HC (2010) Segregation of coarse aggregates in self-compacting concrete. Des Product Place Self-Consol Concr 1:113–125

Roeder CW, Cameron B, Brown CB (1999) Composite action in concrete filled tubes. J Struct Eng 125:477–483

Samani AK, Attard MM (2012) A stress-strain model for uniaxial and confined concrete under compression. Eng Struct 41:335–349

Schnabl S, Planinc I (2019) Circumferential gap and partial debonding effects on buckling loads and modes of slender CFST circular columns. Acta Mech 230:909–928

Schneider SP (1998) Axially loaded concrete-filled steel tubes. J Struct Eng 124:25–38

Tao Z, Uy B, Han LH, Wang ZB (2009) Analysis and design of concrete-filled stiffened thin-walled steel tubular columns under axial compression. Thin-Walled Struct 47:1544–1556

Tao Z, Uy B, Liao FY, Han LH (2011) Nonlinear analysis of concrete-filled square stainless steel stub columns under axial compression. J Constr Steel Res 67:1719–1732

Tao Z, Wang ZB, Qing Y (2013a) Finite element modelling of concrete-filled steel stub columns under axial compression. J Construct Steel Res 89:121–131

Tao Z, Wang XQ, Brian U (2013b) Stress-strain curves of structural and reinforcing steels after exposure to elevated temperatures. J Mater Civil Eng 25:1306–1315

Wang YF, Ma YS, Han B, Deng SY (2013) Temperature effect on creep behavior of CFST arch bridges. J Bridge Eng 18:1397–1405

Xie KZ, Wang HW, Pang JH, Zhou JX (2019) Study of the ultimate bearing capacity of concrete-filled steel tube K-Joints. KSCE J Civil Eng 5:2254–2262

Yan S, Zhang B, Song G, Lin J (2018) PZT-based ultrasonic guided wave frequency dispersion characteristics of tubular structures for different interfacial boundaries. Sensors 18:4111–4133

Ye F, Zha X, Wang H (2011) The application of a HHT based ultrasonic detecting method in quality assessment of CFST. Adv Steel Constr 7:182–191

Yu T, Teng JG, Wong YL, Dong SL (2010a) Finite element modeling of confined concrete-II: plastic-damage model. Eng Struct 32:680–691

Yu T, Teng JG, Wong YL, Dong SL (2010b) Finite element modeling of confined concrete-I: Drucker-Prager type plasticity model. Eng Struct 32:665–679

Zheng J, Wang J (2018) Concrete-filled steel tube arch bridges in China. Eng 4:143–155